PERGAMON

International Journal of Solids and Structures 40 (2003) 1865–1884

INTERNATIONAL JOURNAL OF SOLIDS and STRUCTURES

www.elsevier.com/locate/ijsolstr

Analysis of tapered ENF specimen and characterization of bonded interface fracture under Mode-II loading

Pizhong Qiao [a,*], Jialai Wang [a], Julio F. Davalos [b]

[a] *Department of Civil Engineering, The University of Akron, Akron, OH 44325-3905, USA*

[b] *Department of Civil and Environmental Engineering, West Virginia University, Morgantown, WV 26506-6103, USA*

Received 8 July 2002; received in revised form 6 December 2002

Abstract

An engineering approach for evaluating the shear-mode (Mode-II) fracture toughness of wood–wood and wood-composite bonded interfaces is presented. A tapered beam on elastic foundation model is developed to analyze and design a linear tapered end-notched flexure (TENF) specimen for fracture tests of bonded interfaces. The elastic foundation model is verified numerically by finite element analysis and experimentally by compliance calibration tests, which demonstrate that the present model can accurately predict the compliance and compliance rate-change of the specimen, and with proper design, an approximate constant rate of compliance change with respect to crack length can be achieved. The proposed TENF specimen can be used for Mode-II fracture toughness evaluations with reasonable confidence in the linearity of compliance crack-length relationship. The fracture of wood–wood and wood-composite bonded interfaces under Mode-II loading is experimentally evaluated using the proposed TENF specimen, and the corresponding values of critical strain energy release rate are obtained. The modeling technique and testing method presented can be efficiently used for characterization of Mode-II fracture of bonded bimaterial interfaces.

Keywords: Tapered beam; Elastic foundation; Mode-II fracture; Bonded interface; FRP composites; Compliance calibration; Fracture toughness

1. Introduction

Adhesively bonded joints are effective fastening systems for structural applications. Fiber-reinforced plastic (FRP) composites are being used for reinforcement of wood and concrete, and current research on reinforcement with composites has focused on the use of FRP strips or fiber fabrics adhesively bonded to members. Although significant increases in stiffness and strength have been achieved by this reinforcing technique, there is a concern about the reliable performance of the interface bond, which can be susceptible to delamination. An inadequate interface bond strength and integrity can lead to premature failure of a

* Corresponding author. Address: Department of Civil Engineering, Auburn Science & Engineering Center, Rm, 534, The University of Akron, 244 Sumner Street, Akron, OH 44325-3905, USA. Tel.: +1-330-972-5226; fax: +1-330-972-6020.

E-mail address: qiao@uakron.edu (P. Qiao).

0020-7683/03/$ - see front matter © 2003 Elsevier Science Ltd. All rights reserved.
doi:10.1016/S0020-7683(03)00031-3

reinforced member, and therefore, a need exists to develop efficient test methods to characterize the bond strength of the adherend-FRP interface.

Fracture mechanics concepts are effectively used to simulate the actual fracture response of adhesively bonded structures. An opening tension loading is generally recommended for evaluating adhesively bonded interface strength, since crack extension under Mode-I is more likely than under in-plane shear Mode-II loading. However, for most structural applications of adhesively bonded joints, Mode-II fracture is a major contributor to crack propagations (Mall et al., 1982). For wood or concrete members reinforced with FRP composites, generally applied to the tension side, delamination of the FRP laminate near the ends of adhesively bonded joints may occur due to high shear and peeling stress concentrations. In such a case, the fracture toughness under shear loading is a critical interface property to evaluate the potential crack growth. Therefore, while the opening Mode-I fracture is generally more critical and recommended for qualification of bonded joints, the Mode-II fracture toughness is important for design applications.

The end-notched flexure (ENF) specimen has been widely used to obtain Mode-II fracture toughness, and it is essentially a three-point bending beam with a mid-plane initial crack of a desired length a at one end of the beam. The ENF specimen has received most attention for shear-induced fracture, and extensive studies have been carried out on analysis, modeling, and design of the specimen (Russel and Street, 1982; Carlsson et al., 1986; Corleto and Hogan, 1995; Wang and Qiao, in press). For practical applications, however, the ENF specimen presents some difficulties, such as friction effect, precisely defining an initial crack, and unstable propagation for long crack lengths ($a/L > 0.7$). Moreover, great efforts must be made to measure the crack length during the test, which is particularly a difficult task in testing adhesively bonded joints.

In our previous studies, an efficient specimen, tapered double cantilever beam (TDCB), was analyzed and used for evaluating fracture toughness of wood–FRP bonded interfaces under Mode-I loading (Davalos et al., 1997, 1998a,b; Qiao et al., 2003). The special feature of the TDCB specimen is that there is a relatively linear dependence of compliance with respect to crack length. Consequently, the crack propagates under approximately constant critical fracture loads, and based on the constant compliance rate-change of the specimen, the fracture toughness can be directly obtained by measuring the critical loads for crack initiation and crack arrest without measuring the crack length. In the present study, a similar methodology is adopted, and a new tapered end-notched flexure (TENF) specimen is developed to evaluate the Mode-II fracture toughness of adhesively bonded joints, and by defining the contour, the TENF specimen shows similar linear dependence of compliance with crack length over a certain range of crack length as the TDCB specimen does.

In this study, a combined analytical and experimental approach is used to develop the TENF specimen, and the fracture of hybrid material bonded interfaces under Mode-II loading is characterized. A simple analytical model of the TENF specimen was proposed by Edde and Verrenman (1995); however, their model was based on a simple beam theory, and the shear and crack-tip deformations were not accounted for in the analysis. For specimens made of wood and FRP materials, the shear deformation is relatively significant and should be considered in the design. Studies on the ENF specimen (Wang and Qiao, in press) also indicate that the crack-tip deformation has considerably influence on the total strain energy release rate of the specimen, and therefore, beam theory (Edde and Verrenman, 1995) may underestimate the strain energy release rate of the TENF specimen. In our recent study on the TDCB specimen (Qiao et al., 2003), a tapered beam on elastic foundation (TBEF) model was established to account for the crack-tip deformation. In this study, the TBEF model is extended to analyze and design the TENF specimen, and more accurate expressions of compliance and compliance rate-change are developed. By using the TBEF model, a new and unique TENF specimen is designed so that a relatively constant compliance rate-change can be archived over a certain range of crack length, and combining with experimentally measured critical fracture load, the critical strain energy release rate or fracture toughness of interface bond is evaluated. The nature and configuration of the TENF specimen are different from the ones of the TDCB specimen (Qiao et al.,

2003), and the analytical formulation presented in this study provides a solution of tapered beam with one end notch using the TBEF model. The constant compliance rate change of the TENF specimen is validated with finite element modeling and experimental compliance calibration tests. Several TENF specimens with wood–wood and wood–FRP bonded interfaces are tested under Mode-II loading, and the corresponding interface fracture toughness values are obtained.

2. Analysis of TENF specimen using TBEF model

A conventional approach for determining the fracture toughness of an interface under Mode-II loading is by testing the ENF specimens under central loading of P. The critical strain energy release rate, G_c, which is a measure of the fracture toughness of a bonded interface, is given by Carlsson and Pipes (1987):

$$G_c = \frac{P_c^2}{2b}\frac{dC}{da} \tag{1}$$

where, P_c is the critical load, b is the width of the specimen, and dC/da is the compliance rate-change with respect to crack length a. Tests with conventional constant-height ENF specimens require measurements of crack-length propagation, which are generally difficult to perform. The measurement of crack length can be avoided by contouring the specimen, such that dC/da is a constant, which can be achieved with contoured or tapered (TENF) geometries. Therefore, predicting the compliance accurately and achieving linearity of compliance vs. crack-length relationship are both important in designing and implementing the TENF specimen.

In this section, the theoretical development of a TBEF model is presented for application to TENF specimens consisting of same materials and also different materials for adherend and contour portions. Based on the TBEF formulation, analytical solutions of compliance and compliance rate-change of TENF specimens are obtained. Using a specific example, the accuracy of the analytical model is validated with finite element analyses of tapered beams with different slopes, and the linearity of compliance vs. crack-length relationship is illustrated.

2.1. TENF specimen with same materials for adherend and contour

Consider a typical TENF specimen configuration shown in Fig. 1. The beam is divided into three regions (Fig. 2): a cracked region (I), a linear tapered un-cracked region (II) on the left of the loading point, and a linear tapered un-cracked region on the right of the loading point (III). The upper or lower beam height is a linear function of slope k in regions I, II and III, and is expressed as

$$h(x) = h_0 + kx \quad \text{for } 0 < x < L \tag{2}$$

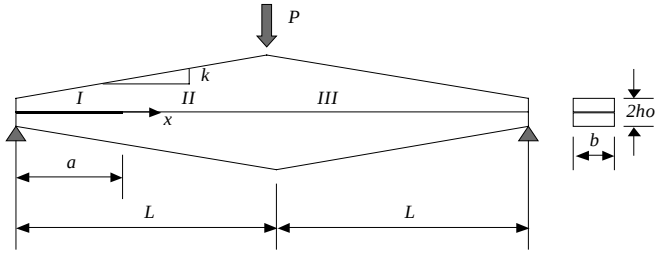

Fig. 1. TENF specimen with same material for adherend and contour.

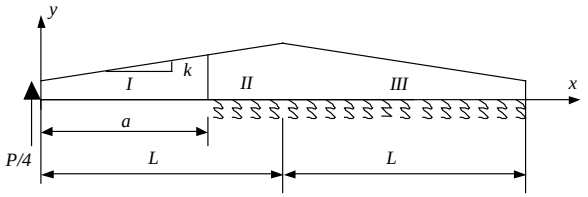

Fig. 2. Model of TENF on generalized elastic foundation.

$$h(x) = h_0 + k(2L - x) \quad \text{for } L < x < 2L \tag{3}$$

In region I ($0 \leqslant x \leqslant a$):

Due to geometrical symmetry of the TENF specimen to the neutral axis (Fig. 1), the deformation of only the upper half beam is analyzed, and the lower half of the beam deforms in the same way. Considering the rotation (ϕ_{I}) of a cross-sectional normal and the transverse beam deflection (w_{I}), the conventional Timoshenko's beam equations including shear deformation for this portion (region I) are defined as

$$M_{\mathrm{I}}(x) = -D_{\mathrm{I}}(x)\frac{\mathrm{d}\phi_{\mathrm{I}}}{\mathrm{d}x} \tag{4}$$

$$\frac{\mathrm{d}w_{\mathrm{I}}}{\mathrm{d}x} - \phi_{\mathrm{I}} = \frac{Q_{\mathrm{I}}(x)}{F_{\mathrm{I}}(x)} \tag{5}$$

where $D_{\mathrm{I}}(x)$ and $F_{\mathrm{I}}(x)$ are the bending and shear stiffnesses of the half beam (Fig. 2), respectively. Considering a beam of width b, moment of inertia I, longitudinal elastic modulus E_1, and shear modulus G, we have

$$D_{\mathrm{I}}(x) = E_1 I(x) \quad F_{\mathrm{I}}(x) = \kappa G b h(x) \tag{6}$$

where, κ is the shear correction factor. Note that the upper half beam is subjected only to half of the shear force at the supporting point (Gillespie et al., 1986), and the moment and shear force can be expressed in terms of the load P as

$$M(x) = -Px/4 \quad Q(x) = -P/4 \tag{7}$$

The simplification and boundary conditions given in Fig. 2 are commonly used in the literature (Gillespie et al., 1986) for the ENF specimen analysis. Based on the results obtained from the finite element analysis (FEA) (Gillespie et al., 1986), the friction between the contact surfaces of upper and lower half beams is minimal, and the reaction forces of upper beam due to lower beam (elastic foundation support) in region II are mainly distributed near the end loading tip and crack tip (i.e., $P/4$). Between the end loading tip and crack tip, the distribution of vertical force is small and neglected in the most ENF specimen analyses.

The generalized displacements (ϕ_{I}, w_{I}) of the cracked region I can be obtained by integrating Eqs. (4) and (5). For region I ($0 \leqslant x \leqslant a$):

$$\phi_{\mathrm{I}} = \frac{3h_0 P}{2Ebk^2h^2} - \frac{3P}{Ebk^2h} + c_1 \tag{8}$$

$$w_{\mathrm{I}} = -\frac{3h_0 P}{2Ebk^3h} - P\left(\frac{1}{4bk\kappa G} + \frac{3}{bEk^3}\right)\log h + c_1 x + c_2 \tag{9}$$

where c_1 and c_2 are the rotation and deflection of the beam at $x = 0$. Similarly, we can obtain the deformation of the regions II and III.

In region II ($a \leqslant x \leqslant L$):

$$\phi_{\mathrm{II}} = \frac{3h_0P}{8Ebk^2h^2} - \frac{3P}{4Ebk^2h} + c_3 \tag{10}$$

$$w_{\mathrm{II}} = -\frac{3h_0P}{8Ebk^3h} - P\left(\frac{1}{4bk\kappa G} + \frac{3}{4bEk^3}\right)\log h + c_3x + c_4 \tag{11}$$

In region III ($L \leqslant x \leqslant 2L$):

$$\phi_{\mathrm{III}} = -\frac{3h_0P}{8Ebk^2h^2} + \frac{3P}{4Ebk^2h} + c_5 \tag{12}$$

$$w_{\mathrm{III}} = -\frac{3h_0P}{8Ebk^3h} - P\left(\frac{1}{4bk\kappa G} + \frac{3}{4bEk^3}\right)\log h + c_5x + c_6 \tag{13}$$

where c_3, c_4, c_5, c_6 are the integration coefficients determined by the boundary conditions, which are defined as:

at both the supporting ends, the vertical deflections are zero, and therefore:

$$w_{\mathrm{I}}(0) = 0 \tag{14}$$

$$w_{\mathrm{III}}(2L) = 0 \tag{15}$$

at the interface of the regions II and III, the continuity conditions give:

$$\phi_{\mathrm{II}}(L) = \phi_{\mathrm{III}}(L) \tag{16}$$

$$w_{\mathrm{II}}(L) = w_{\mathrm{III}}(L) \tag{17}$$

at the crack tip, due to the strain singularity, the rotation and shear deformation of the beam change dramatically. Therefore, the following continuity conditions as suggested in Corleto and Hogan (1995) are employed:

$$w_{\mathrm{I}}(a) = w_{\mathrm{II}}(a) + w_0 \tag{18}$$

$$\phi_{\mathrm{I}}(a) = \phi_{\mathrm{II}}(a) + \phi_0 \tag{19}$$

where ϕ_0 and w_0 are the rotation and vertical displacement at the crack tip caused by the stress and strain singularity.

By substituting the deformation expressions of Eqs. (8)–(13) into the boundary and continuity conditions of Eqs. (14)–(19), the unknown coefficients $c_1, \ldots, c_6$ can be determined and finally the compliance of the TENF specimen is obtained as:

$$C_{\mathrm{II}} = C_{\mathrm{b}} + \frac{1}{2}(\phi_0 a + w_0) \tag{20}$$

where:

$$C_{\mathrm{b}} = \frac{1}{8bE_{11}k^3}\left(A - \left(15 + \frac{2E_{11}k^2}{\kappa G_{12}}\right)\log(h_0) - 9\log(h_a) + \left(9 + \frac{2E_{11}k^2}{\kappa G_{12}}\right)\log(h_L)\right) \tag{21}$$

and

$$A = -4.5 - \frac{h_0(4.5h_0 + 6ka)}{h_a^2} + \frac{h_0(4.5h_0 + 6kL)}{h_L^2} - \frac{6k(2h_0 + 3ka)a}{h_a^2} + \frac{h_0(4.5h_0 + 6kL)k}{h_L^2} \tag{22}$$

$$h_a = h_0 + ka \tag{23}$$

$$h_L = h_0 + kL \tag{24}$$

Note that if we let $w_0 = 0$ in Eq. (18) and $\phi_0 = 0$ in Eq. (19), as commonly used in Edde and Verrenman (1995), we can find that $C_{\mathrm{II}} = C_{\mathrm{b}}$, which is exactly the same as the solution of conventional Timoshenko's beam model for the specimen and corresponds to the deflection at the mid-span of the specimen $w(L)$ under a unit loading P. This indicates that the total compliance of a TENF specimen given in Eq. (20) consists of two parts: (a) the global deformation of the TENF specimen based on Timoshenko's beam theory, C_{b}, and (b) the local crack-tip deformation, $(\phi_0 a + w_0)/2$. Therefore, the crack-tip rotation (ϕ_0) and displacement (w_0) need to be determined so that the compliance of the TENF can be obtained.

2.2. Crack-tip rotation and displacement

To determine the crack-tip rotation and transverse deflection, we model the upper half beam of the TENF specimen with its un-cracked portion supported by an elastic foundation (Fig. 2). Now the problem is to compute the rotation ϕ_0 and vertical displacement w_0 at $x = a$ of the upper half tapered beam under the tip loading of $P/4$ at $x = 0$ and with the elastic foundation support shown in Fig. 2. The un-cracked portion of the TENF specimen is modeled as a half beam on an elastic foundation defined by rotational (k_{r}) and extensional (k_{e}) elastic coefficients. The reaction force $P/4$ acts at the end of the cracked portion. Then the rotation (ϕ_0) and vertical displacement (w_0) at the crack tip ($x = a$) are the unknowns. Based on Timoshenko's beam theory, the governing equations of beam deformations in region II ($a \leqslant x \leqslant L$) are given as

$$\frac{\mathrm{d}}{\mathrm{d}x}\left(D(x)\frac{\mathrm{d}\phi_1}{\mathrm{d}x}\right) + F(x)\left(\frac{\mathrm{d}w_1}{\mathrm{d}x} - \phi_1\right) = k_{\mathrm{r}}\phi_1 \tag{25}$$

$$\frac{\mathrm{d}}{\mathrm{d}x}\left(F(x)\left(\frac{\mathrm{d}w_1}{\mathrm{d}x} - \phi_1\right)\right) = k_{\mathrm{e}}w_1 \tag{26}$$

where, w_1 and ϕ_1 are respectively the displacement and the rotation in region II of the half beam (Fig. 2).

Several ways have been proposed to determine the two foundation elastic coefficients k_{r} and k_{e} (Kanninen, 1973; Williams, 1989; Ozdil and Carlsson, 1999). Generally, they can be expressed in terms of the beam properties as

$$k_{\mathrm{e}} = \frac{nE_2 b}{h(x)} \quad k_{\mathrm{r}} = \frac{\kappa G b h(x)}{n} \tag{27}$$

where n is a dimensionless parameter (Kanninen, 1973) chosen as 2 in this study; E_2 is the Young's modulus perpendicular to the beam axis; and κ is chosen as 5/6 in this study.

Substituting Eq. (25) into Eq. (26), we obtain the expression for w_1 in term of ϕ_1 as:

$$w_1 = \frac{k_{\mathrm{r}}}{k_{\mathrm{e}}}\frac{\mathrm{d}\phi_1}{\mathrm{d}x} - \frac{1}{k_{\mathrm{e}}}\frac{\mathrm{d}^2}{\mathrm{d}x^2}\left(D(x)\frac{\mathrm{d}\phi_1}{\mathrm{d}x}\right) \tag{28}$$

and substituting Eq. (28) into Eq. (25) yields:

$$h^4(x)\frac{\mathrm{d}^4\phi_1}{\mathrm{d}x^4} + 10kh^3(x)\frac{\mathrm{d}^3\phi_1}{\mathrm{d}x^3} + (24k^2 - A)h^2(x)\frac{\mathrm{d}^2\phi_1}{\mathrm{d}x^2} + (12t^3 - A)h(x)\frac{\mathrm{d}\phi_1}{\mathrm{d}x} + B\phi_1 = 0 \tag{29}$$

where

$$A=\frac{1}{k^2}\left(\frac{12\kappa G}{nE}+\frac{nE_2}{\kappa G}\right);\quad B=\frac{12(n+1)E_2}{E}-\frac{12\kappa Gk^2}{nE}$$

As given in Eq. (2), $h(x)$ is a linear function of x, and therefore, the above equation can be rewritten as

$$h^4\frac{\mathrm{d}^4\phi_1}{\mathrm{d}x^4}+10h^3\frac{\mathrm{d}^3\phi_1}{\mathrm{d}x^3}+(24k^2-A)h^2\frac{\mathrm{d}^2\phi_1}{\mathrm{d}x^2}+(12-3A)h\frac{\mathrm{d}\phi_1}{\mathrm{d}x}+\frac{B}{k^4}\phi_1=0 \tag{30}$$

Eq. (30) is an Euler equation, and its characteristic equation can be written as

$$m^4+4m^3+(5-A)m^2+2(1-A)m+\frac{B}{k^4}=0 \tag{31}$$

If Eq. (31) has four real roots m_1, m_2, m_3, and m_4, then the solution can be expressed as

$$\phi_1(x)=A_1h^{m_1}(x)+B_1h^{m_2}(x)+C_1h^{m_3}(x)+D_1h^{m_4}(x) \tag{32a}$$

If Eq. (31) has two pairs of conjugate complex variable roots $m_1\pm \mathrm{i}m_2$ and $m_3\pm \mathrm{i}m_4$, then the solution can be written as

$$\phi_1(x)=h^{m_1}(x)(A_1\cos(m_2\ln(h))+B_1\sin(m_2\ln(h)))+h^{m_3}(x)(C_1\cos(m_4\ln(h))+D_1\sin(m_4\ln(h))) \tag{32b}$$

Substituting the solution of Eq. (32) into Eq. (28), the displacement function $w_1(x)$ can be obtained as:

$$w_1(x)=A_{11}h^{m_1}(x)+B_{11}h^{m_2}(x)+C_{11}h^{m_3}(x)+D_{11}h^{m_4}(x) \tag{33a}$$

where

$$A_{11}=-kh(A_1E_1k^2(m_1+1)(m_1+2)-6\kappa G)/(24E_2)$$

$$B_{11}=-kh(B_1E_1k^2(m_2+1)(m_2+2)-6\kappa G)/(24E_2)$$

$$C_{11}=-kh(C_1E_1k^2(m_3+1)(m_3+2)-6\kappa G)/(24E_2)$$

$$D_{11}=-kh(D_1E_1k^2(m_4+1)(m_4+2)-6\kappa G)/(24E_1)$$

or

$$w_1(x)=\frac{k}{24E_2}h^{m_1+1}(x)(A_{12}\cos(m_2\ln(h))+B_{12}\sin(m_2\ln(h)))+h^{m_3+1}(x)(C_{12}\cos(m_4\ln(h))+D_{12}\sin(m_4\ln(h))) \tag{33b}$$

where

$$A_{12}=A_1\big(-E_1k^2(m_1+1)(m_1^2+2m_1-3m_2^2)+6\kappa Gm_1\big)+B_1\big(-E_1k^2m_2(2+3m_1^2+6m_1-2m_2^2)+6\kappa Gm_2\big)$$

$$B_{12}=A_1\big(E_1k^2m_2(2+3m_1^2+6m_1-m_2^2)-6\kappa Gm_2\big)+B_1\big(-E_1k^2(m_1+1)(m_1^2+2m_1-3m_2^2)+6\kappa Gm_1\big)$$

$$C_{12}=C_1\big(-E_1k^2(m_3+1)(m_3^2+2m_3-3m_4^2)+6\kappa Gm_3\big)+D_1\big(-E_1k^2m_4(2+3m_3^2+6m_3-2m_4^2)+6\kappa Gm_4\big)$$

$$D_{12}=C_1\big(E_1k^2m_4(2+3m_3^2+6m_3-m_4^2)-6\kappa Gm_4\big)+D_1\big(-E_1k^2(m_3+1)(m_3^2+2m_3-3m_4^2)+6\kappa Gm_3\big)$$

In a similar way, the rotation ϕ_2 and displacement w_2 in the region III ($L \leqslant x \leqslant 2L$) can be obtained and expressed as:

$$\phi_2(x) = A_2 h^{m_1}(x) + B_2 h^{m_2}(x) + C_2 h^{m_3}(x) + D_2 h^{m_4}(x) \tag{34a}$$

or

$$\phi_2(x) = h^{m_1}(x)(A_2\cos(m_2\ln(h)) + B_2\sin(m_2\ln(h))) + h^{m_3}(x)(C_2\cos(m_4\ln(h)) + D_2\sin(m_4\ln(h))) \tag{34b}$$

and

$$w_2(x) = A_{21} h^{m_1}(x) + B_{21} h^{m_2}(x) + C_{21} h^{m_3}(x) + D_{21} h^{m_4}(x) \tag{35a}$$

or

$$\begin{aligned} w_2(x) = {} & \frac{k}{24E_2} h^{m_1+1}(x)(A_{22}\cos(m_2\ln(h)) + B_{22}\sin(m_2\ln(h))) \\ & + h^{m_3+1}(x)(C_{22}\cos(m_4\ln(h)) + D_{22}\sin(m_4\ln(h))) \end{aligned} \tag{35b}$$

where

$$A_{21} = -kh(A_2E_1k^2(m_1+1)(m_1+2) - 6\kappa G)$$

$$B_{21} = -kh(B_2E_1k^2(m_2+1)(m_2+2) - 6\kappa G)$$

$$C_{21} = -kh(C_2E_1k^2(m_3+1)(m_3+2) - 6\kappa G)$$

$$D_{21} = -kh(D_2E_1k^2(m_4+1)(m_4+2) - 6\kappa G)$$

$$\begin{aligned} A_{22} = {} & A_2\big(-E_1k^2(m_1+1)(m_1^2+2m_1-3m_2^2) + 6\kappa G m_1\big) \\ & + B_2\big(-E_1k^2m_2(2+3m_1^2+6m_1-2m_2^2) + 6\kappa G m_2\big) \end{aligned}$$

$$B_{22} = A_2\big(E_1k^2m_2(2+3m_1^2+6m_1-m_2^2) - 6\kappa G m_2\big) + B_2\big(-E_1k^2(m_1+1)(m_1^2+2m_1-3m_2^2) + 6\kappa G m_1\big)$$

$$\begin{aligned} C_{22} = {} & C_2\big(-E_1k^2(m_3+1)(m_3^2+2m_3-3m_4^2) + 6\kappa G m_3\big) \\ & + D_2\big(-E_1k^2m_4(2+3m_3^2+6m_3-2m_4^2) + 6\kappa G m_4\big) \end{aligned}$$

$$D_{22} = C_2\big(E_1k^2m_4(2+3m_3^2+6m_3-m_4^2) - 6\kappa G m_4\big) + D_2\big(-E_1k^2(m_3+1)(m_3^2+2m_3-3m_4^2) + 6\kappa G m_3\big)$$

The boundary conditions of the above problem (see Fig. 2) are:

at the crack tip $x = a$:

$$M = -\frac{Pa}{4} \quad Q = -\frac{P}{4} \tag{36}$$

at the right end of the beam ($x = 2L$):

$$M = 0 \quad Q = 0 \tag{37}$$

The continuity conditions at the interface between the region II and III ($x = L$) are:

$$w_1(L) - w_2(L) = 0 \tag{38}$$

$$\phi_1(L) - \phi_2(L) = 0 \tag{39}$$

$$\left.\frac{\mathrm{d}M_1(x)}{\mathrm{d}x}\right|_{x=L} - \left.\frac{\mathrm{d}M_2(x)}{\mathrm{d}x}\right|_{x=L} = 0 \tag{40}$$

$$\left.\frac{\mathrm{d}Q_1(x)}{\mathrm{d}x}\right|_{x=L} - \left.\frac{\mathrm{d}Q_2(x)}{\mathrm{d}x}\right|_{x=L} = 0 \tag{41}$$

where M_i $(i = 1, 2)$ and Q_i $(i = 1, 2)$ are the internal moments and forces in regions II and III, respectively, and defined as:

$$M_i(x) = -E_1 I(x)\frac{\mathrm{d}\phi_i}{\mathrm{d}x} \quad Q_i(x) = \frac{\mathrm{d}}{\mathrm{d}x}(M_i(x)) - k_\mathrm{r}\phi_i \quad i = 1, 2 \tag{42}$$

Considering the above boundary conditions (Eqs. (36)–(41)), we can determine the unknown coefficients in Eqs. (32)–(35). The values of ϕ_0 and w_0, are therefore the corresponding values of ϕ_1 and w_1 at $x = a$, respectively. By using symbolic mathematics software (e.g., Mathematica or Maple), the compliance (C_II) in Eq. (20) and compliance rate-change ($\mathrm{d}C_\mathrm{II}/\mathrm{d}a$) of the specimen can be computed. As an illustration, a numerical example and comparisons with finite element analyses are given in a later section.

2.3. TENF specimen with different materials for adherend and contour

In case of different materials for adherend and contour portions (Fig. 3), the same procedures as before can be applied to the cracked region I, and the corresponding deformation can be obtained; but to account for the different materials for the adherend and contour, the shear and bending stiffnesses of the beam need to be changed correspondingly as

$$D(x) = E_1 I(x) = \frac{bE_\mathrm{c}(2mh_\mathrm{c}h_\mathrm{b}(2h_\mathrm{c}^2 + 3h_\mathrm{b}h_\mathrm{c} + 2h_\mathrm{b}^2) + h_\mathrm{c}^4 + m^2h_\mathrm{b}^4)}{12(h_\mathrm{c} + mh_\mathrm{b})} \tag{43}$$

$$F(x) = \kappa Gbh(x) = b\kappa(G_\mathrm{b}h_\mathrm{b} + G_\mathrm{c}h_\mathrm{c}(x)) \tag{44}$$

where, the subscripts b and c correspond to the base adherend and contour, respectively (Fig. 4), and m is the ratio of adherend to contour Young's moduli ($m = E_\mathrm{b}/E_\mathrm{c}$).

For the un-cracked portion of regions II and III, similar to the analysis presented before, the section is modeled as a beam on elastic foundation. However, it is relatively difficult to get an explicit formula due to the complexity of the stiffness expressions given in Eqs. (25) and (26). Therefore, only the upper contour portion of the hybrid beam is modeled as a beam on elastic foundation, and the thin base adherend is

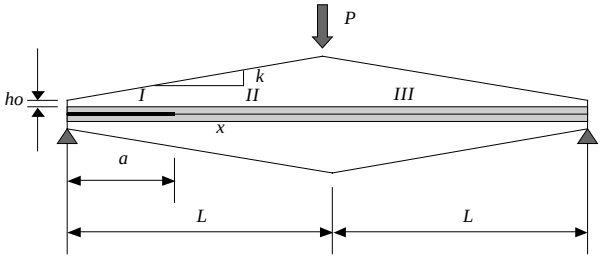

Fig. 3. TENF specimen with different materials for adherend and contour.

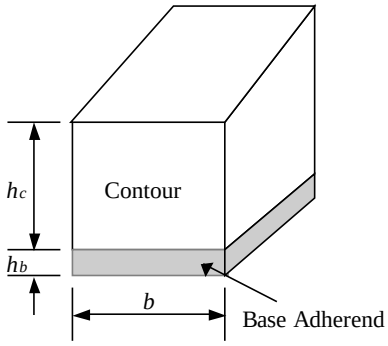

Fig. 4. Tapered beam with different materials for adherend and contour.

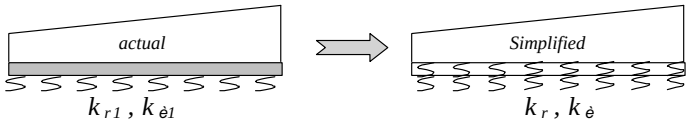

Fig. 5. Elastic foundation model for a hybrid beam.

considered as a part of the elastic foundation (see Fig. 5). Therefore, the foundation elastic coefficients of the base material are simply approximated as:

$$k_{e2} = \frac{E_{b2}b}{h_b} \quad k_{r2} = \kappa G_b b h_b \tag{45}$$

where the subscript b refers to the parameters of the base material, e.g., FRP composites. Note that Eq. (45) is obtained from Eq. (27) by choosing $n = 1$ (note that h_b is the constant thickness of base beam compared to the thickness of half tapered beam $h(x)/2$ or half contoured portion $h_c/2$). By considering both the base and contour portion in the foundation, the elastic coefficients of the foundation can therefore be modified as:

$$k_e = \frac{2E_{c2}b}{h_c\left(1 + \dfrac{2E_{c2}h_b}{E_{b2}h_c}\right)} \quad k_r = \frac{\kappa G_c h_c b}{1 + \dfrac{2G_{c2}h_c}{E_{b2}h_b}} \tag{46}$$

where the subscript c refers to the parameters of contour part of the hybrid beam. Notice that h_c is not a constant here, and to develop a close form solution similar to the procedure in Section 2.1 or 2.2, we approximate h_c as a constant h_0, representing the height at the crack tip. As demonstrated later, this simplified approximation shows satisfactory results. Therefore, the differential equation to obtain the deformation at the crack tip can be established, and the same equations for regions II and III derived in Section 2.1 can be employed. Since only the contour part is taken into consideration (Fig. 5), the first two conditions in Eq. (7) are modified as

$$M(a) = -\frac{E_c b h_c^3}{12D(x)}Pa \quad Q(a) = -\frac{\kappa G_c b h_c}{F(x)}P \tag{47}$$

where $D(x)$ and $F(x)$ are given in Eqs. (43) and (44), respectively. Considering the above modification, an approximate solution for the compliance of the hybrid TENF specimen can be obtained.

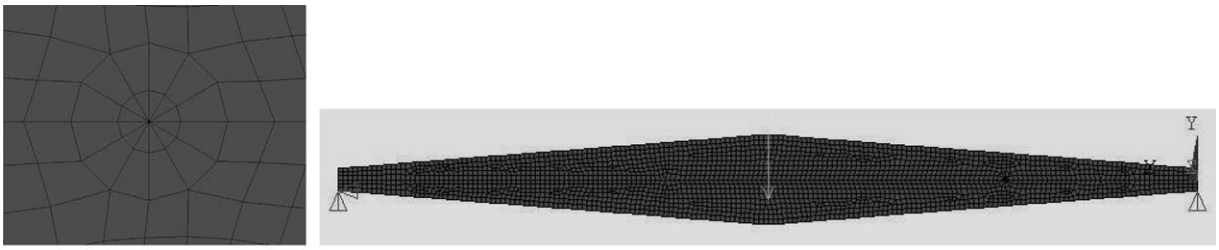

(a) Finite element mesh at crack tip

(b) Entire specimen

Fig. 6. Finite element modeling of TENF specimen.

2.4. Finite element modeling

To verify the TBEF model presented above, finite element analyses are carried out to predict the compliance of the TENF specimen. The commercial finite element program ANSYS with a pre-processor is used. Isoparametric eight-node quadrilateral and six-node triangular plane stress elements are used to automatically generate the mesh. The most important region in the model is the crack tip. According to linear elasticity, the displacements near the crack tip vary as $r^{1/2}$, where r is the distance from the crack tip. As a result, the stresses and strains are singular at the crack tip and proportional to $r^{-1/2}$. A typical way to capture the strain singularity is to use singular elements at the crack tip. To generate a singular element, an eight-node quadrilateral element is collapsed to a triangular element by coalescing nodes along one side first. Then the mid-side node of neighboring is moved to coalescing nodal sides to a quarter point position. Twelve singular elements are used at the crack tip, and the crack surface is modeled as a contact pair (CONTA172 and TARGE169). A section of the finite element model of the TENF specimen is shown in Fig. 6.

2.5. Numerical verification

To verify the accuracy of the proposed TBEF model, the analytical compliance predictions are compared with the numerical results by the FEA. First, the specimen with the same material for the adherend and contour is studied. The dimensions of the specimen are $h_0 = 8.64$ mm (0.34 in.), $L = 0.34$ m (13.4 in.), and

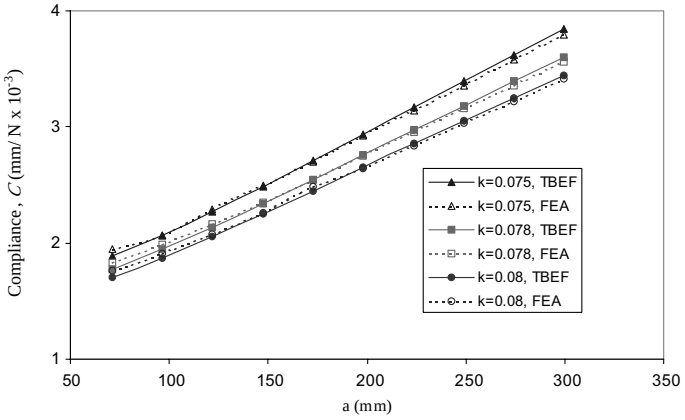

Fig. 7. Comparison of compliances of the TENF specimen made of same material for adherend and contour.

$b = 30.48$ mm (1.20 in.) (see Fig. 1), and the material properties of wood are $E_1 = 13.714$ GPa (1.989×10^6 psi), $E_2 = 0.586$ GPa (0.085×10^6 psi), $G_{12} = 0.689$ GPa (0.1×10^6 psi), and $v_{12} = 0.3$. The compliance values of different slopes with the tapered edges are shown in Fig. 7, and the corresponding compliance rate-change is shown in Fig. 8. The results in Fig. 7 show an excellent agreement for compliance (with a maximum discrepancy of 3.5%) between the TBEF predictions and FEA results. Also, a constant compliance rate-change is obtained within the crack-length range of 152.4 mm (6.0 in.) to 254.0 mm (10.0 in.) (Fig. 8). Similarly, the tapered specimen with different adherend and contour materials is studied. The wood material properties of the contour are the same as for the above example with the initial contour height of $h_0 = 4.699$ mm (0.185 in.), $L = 0.34$ m (13.4 in.), and $b = 30.48$ mm (1.20 in.) (see Fig. 3). The material properties of the constant-thickness ($h_b = 2.54$ mm (0.1 in.)) adherend made of pultruded phenolic FRP strip are: $E_1 = 37.440$ GPa (5.430×10^6 psi), $E_2 = 3.744$ GPa (0.543×10^6 psi), $G_{12} = 5.351$ GPa (0.776×10^6 psi), and $v_{12} = 0.3$. Again, close correlation (with a maximum difference of 2.5%) of compliances between the TBEF model and FEA predictions are obtained (Fig. 9), and a relatively constant compliance rate-change is achieved over the crack range of 152.4 mm (6.0 in.) to 254.0 mm (10.0 in.) (Fig. 10).

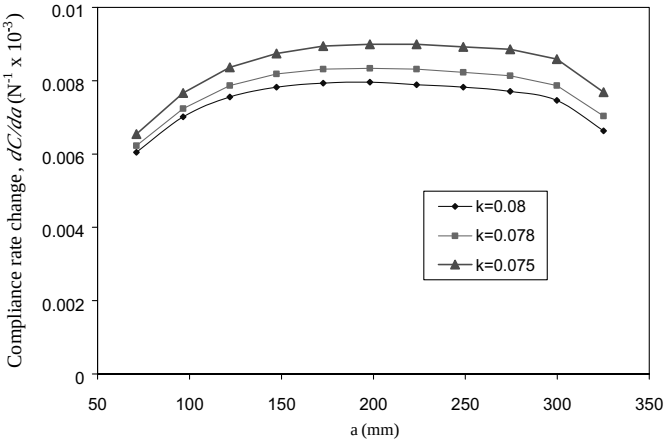

Fig. 8. Compliance change rate of the TENF specimen made of the same material for adherend and contour.

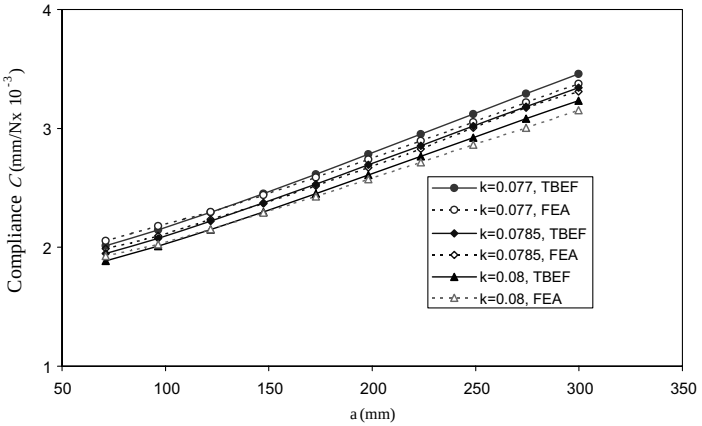

Fig. 9. Comparison of compliances of the TENF specimen made of different materials for adherend and contour.

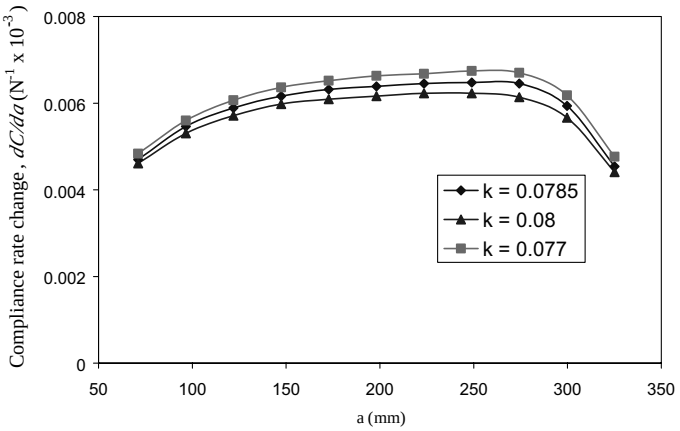

Fig. 10. Compliance change rate of the TENF specimen made of different materials for adherend and contour.

The excellent results for the above two examples indicate that the TBEF can be used with confidence to predict the compliance of the tapered beams, and the constant compliance rate-change shown over a certain range of crack length validates the application of the tapered beam for Mode-II fracture toughness measurements.

2.6. Design of TENF specimen

The compliance of the TENF specimen can be accurately predicted by the TBEF model and defined as a function of the crack length and the slope of the contour. Then the compliance rate-change (dC/da) of the TENF specimen is obtained by differentiating the compliance with respect to the crack length. As shown in Figs. 8 and 10, a properly designed TENF specimen has an approximate linear relationship between the compliance and crack length, i.e., a nearly constant compliance rate-change within a certain range of crack length. The compliance rate-change (dC/da) for all wood specimens with different slopes are shown in Fig. 8, and it is observed that for the slope of the specimen within the give range, e.g., $k = 0.075$–0.080 in this study, the dC/da value remains nearly constant over a crack-length range $a = 152.4$ mm (6.0 in.) to 254.0 mm (10.0 in.).

A similar feature of compliance rate-change is also observed in Fig. 10 for the TENF specimen with different adherend (FRP composite) and contour materials (wood); for the slope range of $k = 0.077$–0.080, the dC/da value for the hybrid materials specimen is nearly constant for crack lengths from 152.4 mm (6.0 in.) to 254.0 mm (10.0 in.).

Therefore, we can conclude that by properly choosing the slope of the tapered specimen, we can obtain a constant compliance rate-change over a certain crack-length range, for which the critical strain energy release rate can be easily evaluated, without the need to measure the crack length in the fracture experiment. The slopes chosen in this study are $k = 0.078$ for the half tapered beam made of wood (Figs. 7 and 8) and $k = 0.0785$ for the half tapered beam made of FRP composite (adherend) and wood (contour) (Figs. 9 and 10).

3. Compliance calibration experiments

To validate the theoretical predictions of compliance (C) and compliance rate-change (dC/da) obtained with the TBEF model, the compliance calibration tests of TENF specimens with wood–wood and

FRP–FRP bonded interfaces are performed. The TENF wood–wood specimens are made of Red Maple; while the FRP specimens are made of Red Maple as contour portions and pultruded phenolic FRP composites as constant-thickness adherends. The material properties of the Red Maple and FRP composite are the same as given in Section 2.5 and were obtained from tension, bending, and torsion tests (Trimble, 1999).

The compliance calibration experiments were performed on an MTS servo hydraulic testing machine, and the experiment was conducted under displacement-controlled mode for a loading rate of 0.508 mm/min (0.02 in./min). A maximum displacement of 5.08 mm (0.20 in.) was applied, and the load and displacement curves were continuously recorded. The deflection of the TENF specimen at the loading point was measured using an MTS crack opening clip gage.

3.1. Calibration of TENF specimen with wood–wood bonded interface

Based on the TBEF model, the wood–wood TENF specimen with linear slope was designed (Fig. 11(a)) and the contour slope of the specimen was accordingly cut. Then the crack tip was defined by sawing the interface to a specified length. Calibration tests were carried out for every 25.4 mm (one inch) interval, from 71.12 mm (2.8 in.) to 299.72 mm (11.8 in.) for two specimens. The results of these tests along with Timoshenko's beam solution (C_b; see the first term in Eq. (20)), the TBEF results of the present study, and the FEA predictions for the specimen with $b = 30.48$ mm (1.2 in.) are shown in Fig. 12, and we can observe

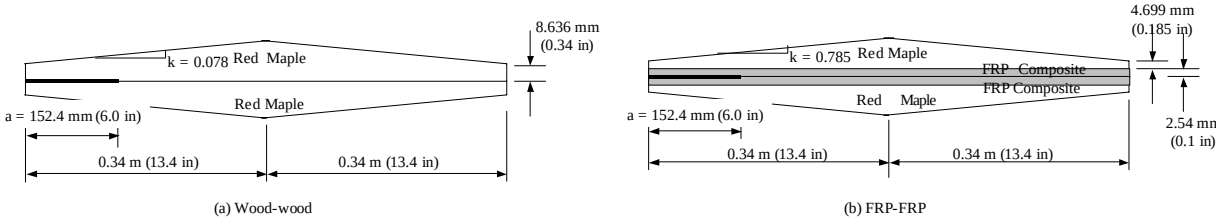

Fig. 11. TENF specimens with wood–wood and FRP–FRP bonded interfaces.

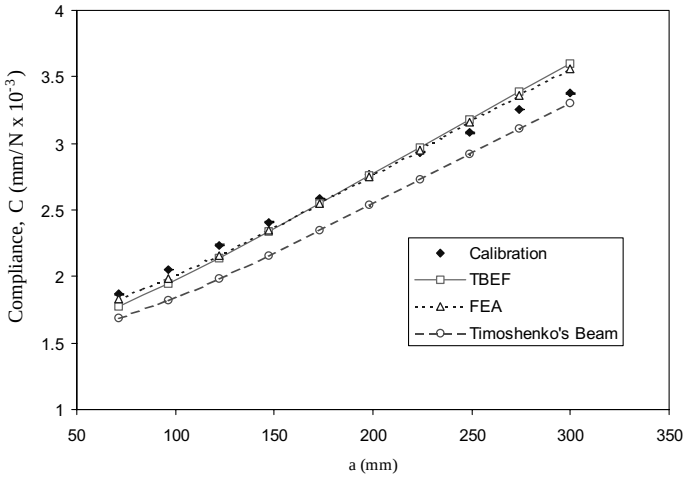

Fig. 12. Compliance calibration of wood–wood bonded interface.

Table 1
Compliance rate-change of the TENF specimens

Specimen	Finite element model 10^{-5} N^{-1} (10^{-5} lb^{-1})	TBEF model 10^{-5} N^{-1} (10^{-5} lb^{-1})	Experimental 10^{-5} N^{-1} (10^{-5} lb^{-1})
Wood–wood	0.794 (3.53)	0.830 (3.69)	0.661 (2.94)
FRP–FRP	0.636 (2.83)	0.639 (2.84)	0.719 (3.20)

that there is a close agreement among the proposed TBEF model, FEA and experimental calibration results. In contrast to the TBEF model, the predictions of the compliance by Timoshenko's beam theory show relatively large discrepancies with the experimental data. The maximum difference between experimental calibration and TBEF prediction is about 6.5% at $a = 299.72$ mm (11.8 in.). There is an apparent linear relationship in Fig. 12 between compliance and crack length within a certain range of crack length (e.g., 147.32 mm (5.8 in.) to 274.32 mm (10.8 in.)). A linear fit of the compliance rate-change for this crack-length range is used to obtain the dC/da values given in Table 1. The experimental dC/da values are lower than expected, which may be caused by the preparation procedures of the specimens; for example, the saw with thickness of 1.016 mm (0.04 in.) used to cut the crack, probably influenced the results. Our tests also indicated that the compliance is quite sensitive to the contour shape, and the deviation of contour shape from the exact design contributes to the difference of compliance rate-change from the expected theoretical and numerical predictions. The material property variation of the wood may also affect the results.

3.2. Calibration of TDCB specimens with FRP–FRP bonded interface

Compliance calibration measurements were also performed on the TENF sample with pultruded phenolic FRP strips as the adherends and Red Maple as the contour portions, as shown in Fig. 11(b). The adhesive used for all face bonding was a Phenol-modified Resorcinol formaldehyde (Penacolite® Resin R-300 and hardener H-30M from Borden Chemicals), which was shown to provide adequate and reliable bonds for wood–wood and wood–FRP interfaces (Davalos et al., 2000a,b). Each FRP adherend was first glued to a rectangular block of Red Maple, and then two blocks with attached FRP adherends were bonded

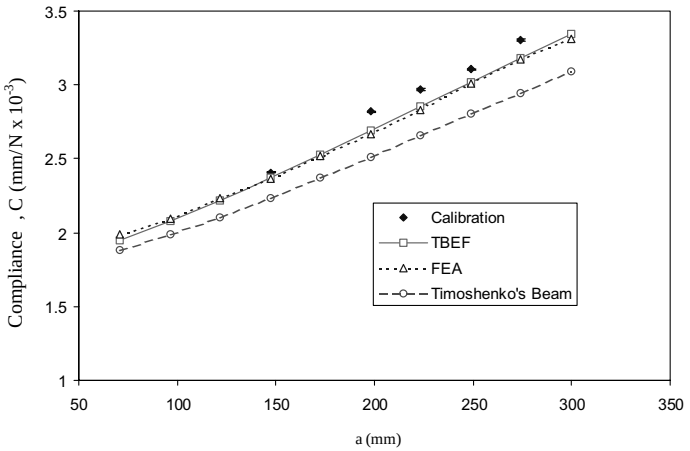

Fig. 13. Compliance calibration of FRP–FRP bonded interface.

together to form the actual interface bond, and the contoured shape on each side was subsequently cut according to the TBEF designed contour. The starting crack length was defined by bonding a cellophane tape on the surfaces of the adherends, prior to bonding the remaining length of the interface. After the compliance was obtained for a particular crack length, the entire bonded interface was fractured (debonded) by applying a cleavage load. The surfaces were then slightly sanded, cleaned and reglued to form a new crack length, which was defined by the length of the tape used on the surface of the adherends.

Since the specimen preparation for each crack length is elaborate, the compliance tests were conducted for crack lengths of 25.4 mm (1.0 in.) increments from 147.32 mm (5.8 in.) to 274.32 mm (10.8 in.), and the results are given in Fig. 13. The TBEF model, experimental calibration, and FEA results show close correlations for both compliance (Fig. 13) and compliance rate-change (Table 1), and the TBEF model gives a better estimate of the compliance compared to the prediction by Timoshenko's beam theory.

4. Fracture toughness of bonded interfaces

The TENF specimens with linear slopes discussed in Section 3 are tested under Mode-II loading to determine the fracture toughness of wood–wood and wood–FRP bonded interfaces (Wang and Qiao, in press). In the experiment, the specimen is loaded to failure to measure the critical loads for crack initiation and crack arrest. Based on the numerical and experimental results discussed above, the TENF specimens are designed to maintain a constant compliance rate-change for a range of crack length. The simultaneous measurement of critical loads for crack initiation and arrest provides a measure of the stability of crack growth. From the critical loads measured, the critical strain energy release rates can be computed from Eq. (1) by using the compliance rate-change determined experimentally and also by the TBEF model.

The TENF specimen of Fig. 11(a) was used to evaluate the fracture toughness of wood–wood bonded interface. As discussed before, this specimen has an approximate constant compliance rate-change for crack lengths beyond 152.4 mm (6.0 in.). Also, the compliance and compliance rate-change of the FRP–FRP specimen of Fig. 11(b) are close to those of the wood–wood specimen (Table 1). Therefore, the specimen used to determine wood–FRP bonded interface fracture toughness (Fig. 14) consists of a half wood–wood specimen (Fig. 11(a)) and a half FRP–FRP specimen (Fig. 11(b)). Since the compliance rate-change is approximately constant for crack lengths beyond 152.4 mm (6.0 in.) for both the wood–wood and FRP–FRP specimens, the wood–FRP specimens were manufactured with an initial crack length of 152.4 mm (6.0 in.). The average values of compliance rate-change of wood–wood and FRP–FRP specimen (Table 1) are used as the compliance rate-change for the wood–FRP specimen. The fracture toughness under Mode-II load were determined by testing the TENF specimens under displacement control mode with a loading rate of 0.610 mm/min (0.024 in./min). The load was applied continuously while crack initiations and arrests were recorded. Since the compliance rate-change (dC/da) was already established for the test specimens, as

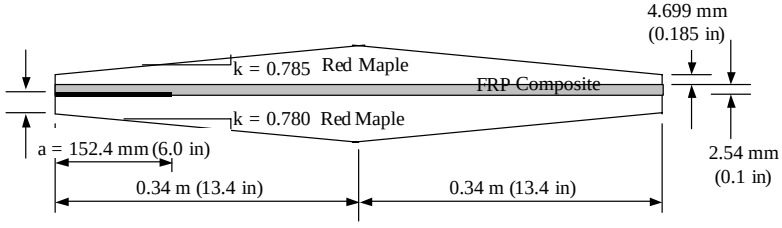

Fig. 14. TENF specimen with wood–FRP hybrid bonded interface.

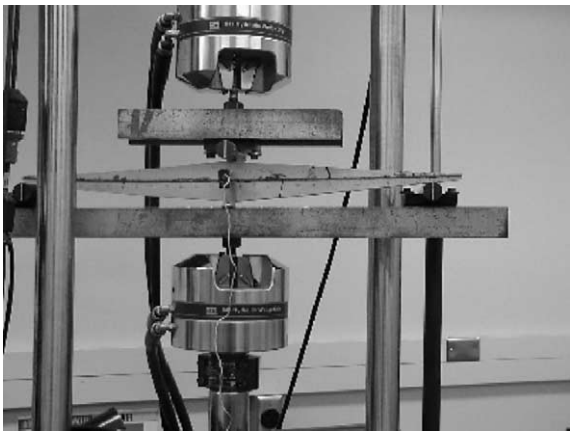

Fig. 15. Testing setup of TENF specimen for Mode-II Fracture.

discussed in Sections 2 and 3, only the critical loads were measured to determine the fracture toughness by Eq. (1). The load point displacement of the specimen was also recorded to show load–displacement relationships.

Six specimens for wood–wood interface and eight specimens for wood–FRP interface were manufactured and tested under Mode-II loading (Fig. 15) to obtain critical loads. Representative results for each interface type are shown in Figs. 16 and 17. A close-up of critical loads for crack initiation and arrest of wood–wood interface is illustrated in Fig. 18. Initially, the elastic strain energy stored in the specimen increases until it reaches the energy required to initiate the crack, which is characterized by a drop in the applied load (Figs. 16–18), and thus, each peak load value corresponds to the critical load of crack initiation. As the crack extends, the applied load is relaxed and the stored elastic strain energy decreases, resulting in crack arrest without complete fracture of the specimen; then, the applied load increases once again. The critical load values at which the load–displacement curves show downward peaks are the critical loads for crack arrest. As noted in Fig. 17, the reciprocal of the slope of the load–displacement curve is the compliance of the specimen. Therefore, the compliance of the specimen can be obtained as $1/k_1$ or $1/k_2$ (see Fig. 17). Compared with the compliance values of experimental calibration or TBEF model, it is found that

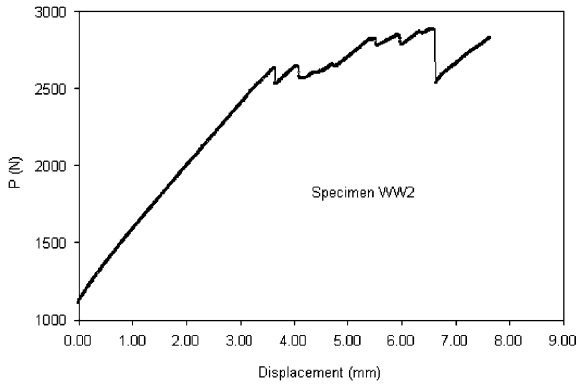

Fig. 16. Load vs. load point displacement for wood–wood (WW) bonded sample.

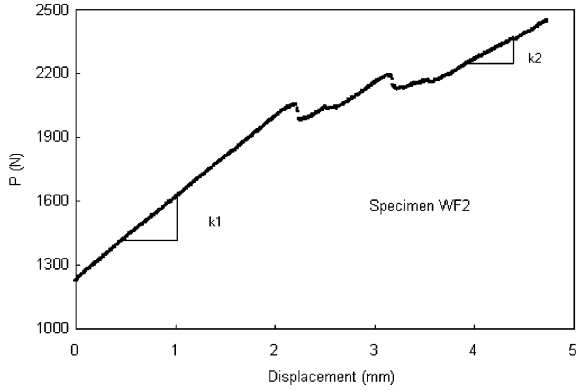

Fig. 17. Load vs. load point displacement for wood–FRP (WF) bonded sample.

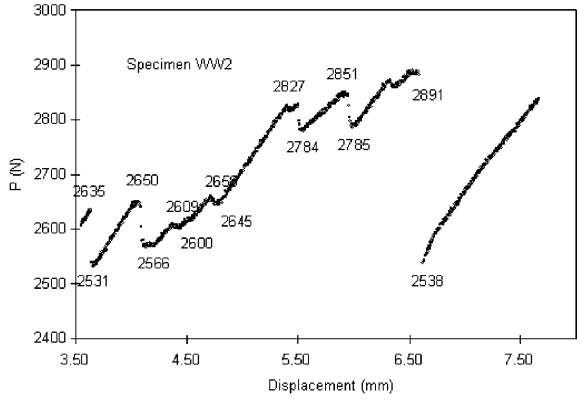

Fig. 18. Details of critical loads for crack initiation and arrest of wood–wood bonded interface.

the crack length under some higher critical loads already goes beyond the constant dC/da region as designed. Therefore, any critical loads in the region where the crack length is greater than the designed region (i.e., from 152.4 mm (6.0 in.) to 254.0 mm (10.0 in.)) are excluded in the analysis (Wang and Qiao, in press).

A statistical analysis of the critical loads yields a mean crack-initiation load value of 2931.8 N (659.1 lb) (COV = 10.1%) and a mean crack-arrest load value of 2827.3 N (635.6 lb) (COV = 11.6%) for the wood–wood bonded interface; whereas for the wood–FRP bonded interface, the mean values of the crack-initiation load of 2242.3 N (504.1 lb) (COV = 9.8%) and crack-arrest load of 2175.2 (489.0 lb) (COV = 9.7%) are obtained. The mean values of the critical loads for the wood–FRP bonded interface are less than the corresponding values obtained for the wood–wood bonded interface. This difference is a consequence of bonding two different adherends with distinct characteristics, resulting in lower bond strength. The mean values of the critical loads and the compliance rate-change obtained experimentally or analytically (Table 1) are substituted in Eq. (1) to determine the critical strain energy release rates for crack initiation and arrest (Table 2). As a comparison, the strain energy release rates for Mode-I fracture toughness of the same bonded interfaces obtained in (Qiao et al., 2000) are also presented in Table 2. We can observe that the strain energy release rates of bonded interfaces under Mode-II loading are greater than the corresponding values for the same interfaces under Mode-I loading.

Table 2
Critical strain energy release rates of interface bonds

Interface	Crack propagation	G_{IIc}, TBEF[a] N/m (lb/in.)	G_{IIc}, Experimental[b] N/m (lb/in.)	G_{Ic} (Qiao et al., 2000) N/m (lb/in.)
Wood–wood	Crack initiation	884.39 (5.05)	1112.06 (6.35)	586.68 (3.35)
	Crack arrest	824.85 (4.71)	1038.50 (5.93)	339.75 (1.94)
Wood–FRP	Crack initiation	586.68 (3.35)	542.89 (3.10)	224.16 (1.28)
	Crack arrest	553.40 (3.16)	511.37 (2.92)	185.63 (1.06)

[a] Based on the dC/da values predicted by the TBEF model.
[b] Based on the experimental dC/da values.

5. Conclusions

In this paper, a TBEF model, which accounts for the crack-tip displacement and rotation, is developed to analyze and model the TENF specimen for Mode-II fracture of bonded interfaces. Based on the TBEF model, a linear relationship between compliance and crack length within a certain crack range is obtained for the TENF specimen. The accuracy of this model and the linearity of the compliance crack-length relationship are verified by finite element analyses and experimental compliance calibration tests for wood–wood and FRP–FRP specimens. Close correlations of compliance and compliance rate-changes between the TBEF model and FEA are achieved. The comparisons of the TBEF model with compliance calibration experiments also indicate that the present model can be used with confidence to predict both the compliance and compliance rate-change, and by using the proposed analytical model, one can alleviate the necessity for extensive experimental compliance calibration tests. It is shown that the linear tapered specimen can be used for fracture toughness tests under Mode-II loading with reasonable confidence in the linearity of the compliance crack-length relationship. The fracture of wood–wood and wood–FRP bonded interfaces under Mode-II loading is experimentally evaluated using the proposed TENF specimens, and the corresponding critical strain energy release rate values G_{IIc} are obtained. The modeling technique and testing method presented can be effectively used to evaluate the fracture toughness of hybrid material bonded interface (e.g., wood–FRP interfaces) under Mode-II loading.

Acknowledgements

Partial financial support for this study was received from the National Science Foundation (CSM-0002829 under program director Dr. Ken P. Chong); the College of Engineering at The University of Akron; and the West Virginia University Research Corporation Incentive Grant Program.

References

Carlsson, L.A., Pipes, R.B., 1987. Experimental Characterization of Advanced Composite Materials. Prentice Hall, Englewood Cliffs, NJ.

Carlsson, L.A., Gillespie Jr., J.W., Pipes, R.B., 1986. On the analysis and design of end notched flexure (ENF) for mode II testing. Journal of Composite Materials 20, 594–604.

Corleto, C.R., Hogan, H.A., 1995. Energy release rates for the ENF specimen using a beam on an elastic foundation. Journal of Composite Materials 29, 1420–1436.

Davalos, J.F., Madabhusi-Raman, P., Qiao, P.Z., 1997. Characterization of Mode-I fracture of hybrid material interface bonds by contoured DCB specimens. Engineering Fracture Mechanics 58 (3), 172–192.

Davalos, J.F., Qiao, P.Z., Madabhusi-Raman, P., Lang, E.M., 1998a. Mode-I fracture toughness of fiber reinforced composite-wood bonded interfaces. Journal of Composite Materials 32 (10), 987–1013.

Davalos, J.F., Madabhusi-Raman, P., Qiao, P.Z., Wolcott, M.P., 1998b. Compliance rate change of tapered double cantilever beam specimen with hybrid interface bonds. Theoretical and Applied Fracture Mechanics 29, 125–139.

Davalos, J.F., Qiao, P.Z., Trimble, B.S., 2000a. Fiber-reinforced composite and wood bonded interface, Part 1. Durability and shear strength. ASTM Journal of Composites Technology and Research 22 (4), 224–231.

Davalos, J.F., Qiao, P.Z., Trimble, B.S., 2000b. Fiber-reinforced composite and wood bonded interface, Part 2. Fracture. ASTM Journal of Composites Technology and Research 22 (4), 232–240.

Edde, F.C., Verrenman, Y., 1995. Nominally constant strain energy release rate specimen for the study of Mode II fracture and fatigue in adhesively bonded joints. International Journal of Adhesion and Adhesives 15, 29–32.

Gillespie, J.W., Carlsson, L.A., Pipes, R.B., 1986. Finite element analysis of the end notched flexure specimen for measuring Mode II fracture toughness. Composite Science and Technology 27, 177–197.

Kanninen, M.F., 1973. An augmented double cantilever beam model for studying crack length propagation and arrest. International Journal of Fracture 9 (1), 83–92.

Mall, S., Johnson, W.S., Everett, R.A., 1982. Cyclic debonding of adhesively bonded composites. NASA Tech. Memo. 84577, National Aeronautics and Space Administration, Washington, DC, 21 p.

Ozdil, F., Carlsson, L.A., 1999. Beam analysis of angle-ply laminate DCB specimens. Composites Science and Technology 59, 305–315.

Qiao, P.Z., Davalos, J.F., Trimble, B.S., 2000. Effect of moisture on fracture toughness of composite/wood bonded interfaces. In: Fatigue and Fracture Mechanics. In: Halford, G.R., Gallagher, (Eds.), ASTM STP 1389, vol. 31. American Society for Testing and Materials, West Conshohochen, PA, pp. 526–544.

Qiao, P.Z., Wang, J.L., Davalos, J.F., 2003. Tapered beam on elastic foundation model for compliance rate change of TDCB specimen. Engineering Fracture Mechanics 70 (2), 339–353.

Russel, A.J., Street, K.N., 1982. Factors affecting the interlaminar fracture energy of graphite/epoxy laminates. Progress in Science and Engineering of Composites. Proceedings of ICCM-IV, Tokyo, pp. 279–286.

Trimble, B.S., 1999. Durability and Mode-I Fracture of Fiber-Reinforced Plastic (FRP)/Wood Interface Bond. Master of Science Thesis, Civil and Environmental Engineering, West Virginia University, Morgantown, WV, 192 p.

Wang, J.L., Qiao, P.Z. Novel beam analysis of end notched flexure specimen for Mode II fracture. Engineering Fracture Mechanics, in press.

Wang, J.L., Qiao, P.Z. Fracture toughness of wood–wood and wood–FRP bonded interfaces under Mode-II loading. Journal of Composite Materials, in press.

Williams, J.C., 1989. End correction for orthotropic DCB specimens. Composites Science and Technology 35 (4), 35–367.